Site-selective spectroscopy and crystal-field analysis for Nd^{3+} in strontium fluorovanadate

Cite as: Journal of Applied Physics **77**, 270 (1995); https://doi.org/10.1063/1.359387
Submitted: 23 May 1994 . Accepted: 18 September 1994 . Published Online: 04 June 1998

R. E. Peale, P. L. Summers, H. Weidner, B. H. T. Chai, and C. A. Morrison

Site-selective spectroscopy and crystal-field analysis for Nd^{3+} in strontium fluorovanadate

R. E. Peale,[a] P. L. Summers, and H. Weidner
Department of Physics, University of Central Florida, Orlando, Florida 32816

B. H. T. Chai
Center for Research and Education in Optics and Lasers (CREOL), University of Central Florida, Orlando, Florida 32826

C. A. Morrison
U.S. Army Research Laboratory, Adelphi, Maryland 20783-1197

(Received 23 May 1994; accepted for publication 18 September 1994)

Site-selective spectroscopy reveals that Nd^{3+} ions occupy more than 40 different crystal-field environments in $Sr_5(VO_4)_3F$. Preferential energy transfer to the site responsible for 1 μm lasing occurs but becomes less complete with increasing temperature. The ^4I and $^4F_{3/2}$ Stark levels of the lasing site have been determined and an analysis of the crystal field performed. From the crystal-field fitting parameters B_{kq}, a calculated energy-level spectrum is determined up to 17 500 cm^{-1} with a rms deviation from the available experimental levels of 6 cm^{-1}. © *1995 American Institute of Physics.*

I. INTRODUCTION

Spectroscopy and laser performance studies show that Nd^{3+}:$Sr_5(VO_4)_3F$ (Nd:SVAP) has promise as the medium for a low pumping-power (<100 mW) microchip laser.[1-3] It can be grown in large sizes with low scattering loss and has high emission cross section, an adequate lifetime, low threshold, and high slope efficiency. SVAP is generally interesting as a host, because the similar crystal SFAP [$Sr_5(PO_4)_3F$] doped with Yb has recently been identified as having the best combination of properties for the solid-state-laser driver of an inertial confinement fusion power reactor.[4]

In this paper, we report our spectroscopic characterization of high quality Nd:SVAP crystals. We find that a large number of distinct crystal-field environments are occupied by Nd^{3+} ions, which most likely results from a variety of configurations taken by the charge compensating defects required for Nd^{3+} ions substituting on a Sr^{2+} site. Multiple crystal-field environments are generally considered a disadvantage for laser crystals, since different Nd ions can have different spectroscopic and dynamic characteristics. For example, some Nd^{3+} ions may passively absorb pump energy without contributing to lasing and some may act as quenching centers. Hence, the role of multiple sites in Nd:SVAP needs to be explored.

In this paper we probe this question by testing two hypotheses. These are: (1) the variety and/or occupation of the possible crystal-field environments decreases with increasing concentration, so that in actual high concentration ($\geq$1%) laser crystals the multiple environments are unimportant; (2) efficient energy transfer to a single environment (the main site) causes the absorption of all (or most) of the Nd^{3+} ions to contribute to the population of the upper laser level. Each hypotheses is a possible explanation for the good lasing[3] in 1% Nd:SVAP.

We find that the first hypothesis is false and that the second is true. We also find that transfer to the main site becomes less complete as the temperature is increased from 2 K. We show that this gives a possible loss mechanism for this otherwise excellent laser crystal.

Our site selective technique has permitted a determination of all of the main site's ^4I_J and $^4F_{3/2}$ Stark levels. A crystal-field calculation has been performed assuming that the site symmetry is C_{1h}, i.e., identical to the symmetry of the lasing site in the isostructural fluorapatite $Ca_5(PO_4)_3F$ or FAP. The 14 B_{kq} fitting parameters required for this symmetry have been determined from a fit involving 28 levels. A calculated energy level spectrum up to 17 500 cm^{-1} differs from the available experimental one with an rms deviation of only 6 cm^{-1}.

II. EXPERIMENT

SVAP crystals were grown by the conventional Czochralski technique at CREOL. Nominal Nd concentrations were 0.2, 1, 1.5, 2, and 4 at. %, as determined by the amount of dopant added to the melt. Actual concentrations (microprobe analysis) were 0.05, 0.26, 0.38, 0.48, and 0.71%, respectively.[3] The discrepancy results presumably from differences in size and charge between Nd^{3+} and the Sr^{2+} ions it replaces.

Absorption and emission spectra were collected with a Bomem DA8 Fourier spectrometer at 1 cm^{-1} resolution. Site-selective cw excitation was achieved with an Ar-laser-pumped jet-dye laser. The laser frequency was determined for each measurement by directly resolving the ~1 cm^{-1} FWHM laser line with the spectrometer. These data also permit correction of excitation spectra for laser power. Samples were cooled to 2 K by immersion in superfluid helium within a Janis supervaritemp optical cryostat with quartz windows or to 80 K with a liquid-nitrogen cold-finger cryostat. Both cryostats are interfaced with the vacuum sample compartment of the spectrometer. All frequencies determined are therefore in vacuum wave numbers.

[a]E-mail: rep@physics.ucf.edu

 0021-8979/95/77(1)/270/7/$6.00

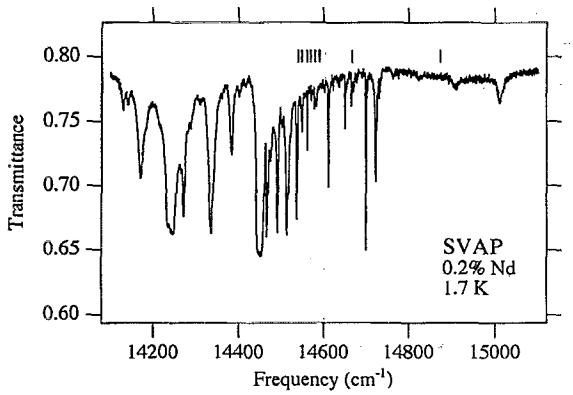

FIG. 1. $^4I_{9/2}\rightarrow{}^4F_{9/2}$ transmittance spectrum of Nd:SVAP. Marks indicate excitation frequencies for the photoluminescence spectra plotted in Fig. 2.

The $^4I_{9/2}\rightarrow{}^4F_{9/2}$ transmittance spectrum at 1.7 K is presented in Fig. 1. The presence of at least 30 lines indicates at least six different crystal-field environments for Nd^{3+} in SVAP. Figure 2 presents a portion of the $^4F_{3/2}\rightarrow{}^4I_{11/2}$ emission spectrum at 2 K for the excitation frequencies given and indicated in Fig. 1 by markers. Evidently, tuning the laser over even a small portion of the $^4F_{9/2}$ band produces a tremendous variety of photoluminescence peaks. All of the various peaks in Fig. 2 change strength independently with changes in excitation frequency. Therefore, each line arises from a unique crystal-field environment. The 15 prominent lines in Fig. 2 imply at least 15 significantly occupied environments in SVAP. Analysis of weak features for a larger number of excitation frequencies than presented in Fig. 2 shows that in fact more than 40 different crystal-field environments exist. Each independent emission spectrum consists primarily of a single sharp line. The excitation has been tuned over the high-frequency half of the $^4F_{9/2}$ absorption band, as permitted by the range of our DCM dye. Hence, significantly more than 40 environments may exist.

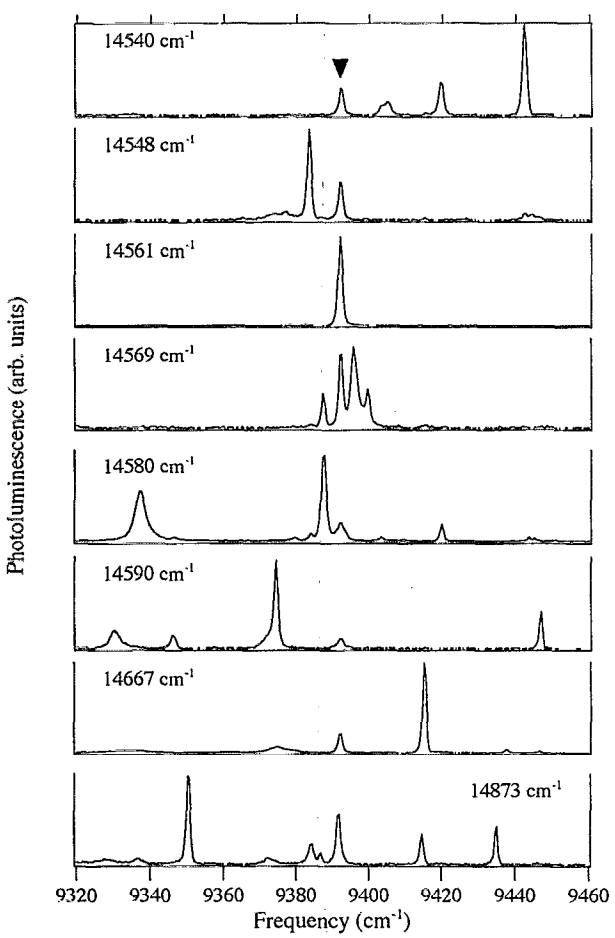

FIG. 2. Portion of the $^4F_{3/2}\rightarrow{}^4I_{11/2}$ luminescence spectrum from Nd:SVAP for different excitation frequencies, as printed in each spectrum and marked in Fig. 1. The sample temperature was 2 K, and the nominal concentration 0.2%. The arrow indicates the main site emission line at the lasing frequency.

Note that a single line (indicated by a symbol) is common to each spectrum in Fig. 2. This line dominates most of our site-selective spectra. (The spectra in Fig. 2 were chosen to convey an impression of the variety of possible results. These spectra are only a small subset of the total number collected.) It shifts from 9392 cm^{-1} at 2 K to 9386 cm^{-1} at 300 K, a value identical to the reported 300 K laser frequency (1.065 μm).[3] The corresponding crystal-field environment will be designated as the "main site" hereafter.

From those $^4F_{3/2}\rightarrow{}^4I_J$ spectra in which main site luminescence dominates, we determine all main site ^4I_J levels and its lowest $^4F_{3/2}$ level. These values are given in Table I. The upper $^4F_{3/2}$ level listed is identified in experiments described below.

Table I permits identification of the lowest main site line in the $^4I_{9/2}\rightarrow{}^4F_{3/2}$ absorption spectrum. Figure 3 presents this spectrum for two samples at 1.7 K with nominal concentrations of 0.2% and 4%. The main site is the strong lowest-frequency feature indicated by the solid square symbol. Other features are correlated with the main site by comparing integrated absorption coefficients for the various bands in a number of samples with differing concentrations. Symbols above the distinct lines or groups of overlapping lines label the features which we have integrated for this comparison.

Figure 4 plots the integrated absorption versus nominal concentration for those features indicated in Fig. 3. The symbols used in the two figures are the same. Features indicated by solid symbols vary in strength similarly with changes in nominal concentration, suggesting that all these features are associated with the main site (including the unresolved shoulders on the line under the solid diamond in Fig. 3).

Since only two $^4I_{9/2}\rightarrow{}^4F_{3/2}$ transitions are expected from a single site, it is of interest to test if any of these correlations are accidental. To do this, we tuned the dye laser (LDS dye) across the features labeled by the solid triangle and diamond (including shoulders) and spectrally resolved the resulting emission. A spectrum of the laser emission was also measured at each step to verify single-mode operation, to accurately determine the excitation frequency, and to give a measure of laser intensity. The intensity of main site emission was determined by integrating the strong main line at 9392 cm^{-1} (indicated by the symbol in Fig. 2). This intensity was divided by the integral of the laser spectrum to correct for changes in laser power with changes in frequency. The re-

TABLE I. Calculated and experimental energy levels (cm^{-1}) for Nd^{3+}:$Sr_5(VO_4)_3F$.[a]

No.	State[b]	Energy (Calc.)	Energy (Exp.)	Free-ion mixture (%)
1	$^4I_{9/2}$	8.3	0	98.49 $^4I_{9/2}$+1.38 $^4I_{11/2}$+0.07 $^4I_{13/2}$
2	468.5	439.8	446.4	99.34 $^4I_{9/2}$+0.43 $^4I_{11/2}$+0.12 $^4G_{5/2}$
3		490.7	495.8	99.45 $^4I_{9/2}$+0.28 $^4I_{11/2}$+0.16 $^4G_{5/2}$
4		547.6	550.4	99.38 $^4I_{9/2}$+0.43 $^4I_{11/2}$+0.09 $^4G_{5/2}$
5		671.7	665.3	98.97 $^4I_{9/2}$+0.88 $^4I_{11/2}$+0.06 $^4G_{5/2}$
6	$^4I_{11/2}$	1896.3	1889.3	97.71 $^4I_{11/2}$+1.66 $^4I_{13/2}$+0.54 $^4I_{9/2}$
7	2321.5	2311.5	2315.4	98.33 $^4I_{11/2}$+1.38 $^4I_{9/2}$+0.20 $^4I_{13/2}$
8		2353.3	2353.1	99.36 $^4I_{11/2}$+0.24 $^4I_{13/2}$+0.21 $^4I_{9/2}$
9		2388.2	2388.3	98.75 $^4I_{11/2}$+0.70 $^4I_{9/2}$+0.38 $^4I_{13/2}$
10		2410.9	2408.5	99.24 $^4I_{11/2}$+0.37 $^4I_{13/2}$+0.24 $^4I_{9/2}$
11		2477.5	2483.1	98.95 $^4I_{11/2}$+0.61 $^4I_{13/2}$+0.32 $^4I_{9/2}$
12	$^4I_{13/2}$	3806.5	3804.1	98.29 $^4I_{13/2}$+1.28 $^4I_{15/2}$+0.35 $^4I_{11/2}$
13	4284.7	4249.0	4257.7	98.01 $^4I_{13/2}$+1.68 $^4I_{11/2}$+0.22 $^4I_{15/2}$
14		4307.7	4303.2	99.29 $^4I_{13/2}$+0.38 $^4I_{11/2}$+0.21 $^4I_{15/2}$
15		4342.1	4349.5	99.44 $^4I_{13/2}$+0.28 $^4I_{15/2}$+0.13 $^4I_{11/2}$
16		4371.0	4374.4	99.43 $^4I_{13/2}$+0.40 $^4I_{15/2}$+0.05 $^4I_{11/2}$
17		4390.5	4383.4	98.81 $^4I_{13/2}$+0.55 $^4I_{11/2}$+0.51 $^4I_{15/2}$
18		4485.1	4479.8	99.22 $^4I_{13/2}$+0.38 $^4I_{15/2}$+0.30 $^4I_{11/2}$
19	$^4I_{15/2}$	5704.3	5718.0	99.58 $^4I_{15/2}$+0.33 $^4I_{13/2}$+0.03 $^4I_{11/2}$
20	6301.5	6232.6	6237.9	99.06 $^4I_{15/2}$+0.81 $^4I_{13/2}$+0.04 $^4F_{9/2}$
21		6256.8	6252.2	99.30 $^4I_{15/2}$+0.55 $^4I_{13/2}$+0.05 $^4F_{9/2}$
22		6315.3	6304.7	99.46 $^4I_{15/2}$+0.42 $^4I_{13/2}$+0.03 $^4I_{11/2}$
23		6379.9	6375.4	99.59 $^4I_{15/2}$+0.28 $^4I_{13/2}$+0.05 $^4F_{7/2}$
24		6405.8	6397.6	99.54 $^4I_{15/2}$+0.24 $^4I_{13/2}$+0.07 $^4F_{9/2}$
25		6502.7	6505.7	99.47 $^4I_{15/2}$+0.35 $^4I_{13/2}$+0.04 $^4I_{11/2}$
26		6616.0	6622.0	99.53 $^4I_{15/2}$+0.31 $^4I_{13/2}$+0.05 $^4F_{9/2}$
27	$^4F_{3/2}$	11286.1	11281.6	94.55 $^4F_{3/2}$+4.19 $^4F_{5/2}$+0.55 $^4F_{7/2}$
28	11556.1	11602.5	11607.0	93.23 $^4F_{3/2}$+4.23 $^4F_{5/2}$+1.29 $^4G_{5/2}$
29	$^4F_{5/2}$	12351.3	···	80.37 $^4F_{5/2}$+9.74 $^2H_{9/2}$+5.07 $^4F_{7/2}$
30	(12573.2)	12497.0	···	80.61 $^4F_{5/2}$+13.36 $^2H_{9/2}$+3.25 $^4F_{3/2}$
31	$+^2H_{9/2}$	12516.8	···	91.14 $^2H_{9/2}$+7.56 $^4F_{5/2}$+0.45 $^4F_{9/2}$
32	(12737.7)	12571.9	···	51.81 $^2H_{9/2}$+46.55 $^4F_{5/2}$+0.54 $^4G_{5/2}$
33		12658.5	···	78.36 $^2H_{9/2}$+19.06 $^4F_{5/2}$+1.47 $^4F_{3/2}$
34		12764.0	···	80.82 $^2H_{9/2}$+17.22 $^4F_{5/2}$+1.16 $^4F_{7/2}$
35		12841.3	···	71.67 $^2H_{9/2}$+26.25 $^4F_{5/2}$+1.45 $^4F_{7/2}$
36		13010.7	···	97.67 $^2H_{9/2}$+1.30 $^4F_{5/2}$+0.49 $^4F_{9/2}$
37	$^4S_{3/2}$	13333.5	···	91.87 $^4F_{7/2}$+2.94 $^4F_{5/2}$+2.68 $^4F_{9/2}$
38	(13459.4)	13423.5	···	96.60 $^4S_{3/2}$+2.42 $^4F_{7/2}$+0.35 $^4G_{5/2}$
39	$+^4F_{7/2}$	13449.6	···	71.95 $^4F_{7/2}$+22.08 $^4S_{3/2}$+2.74 $^4F_{5/2}$
40	(13564.4)	13476.4	···	78.47 $^4S_{3/2}$+19.22 $^4F_{7/2}$+0.99 $^4F_{5/2}$
41		13550.8	···	95.28 $^4F_{7/2}$+1.91 $^4F_{9/2}$+0.85 $^4F_{5/2}$
42		13879.2	···	96.40 $^4F_{7/2}$+1.44 $^2H_{9/2}$+0.89 $^2G_{7/2}$
43	$^4F_{9/2}$	14583.8	···	97.46 $^4F_{9/2}$+1.13 $^4F_{7/2}$+0.62 $^4F_{5/2}$
44	(14854.1)	14768.7	···	95.67 $^4F_{9/2}$+3.53 $^4F_{7/2}$+0.34 $^2H_{11/2}$
45		14927.2	···	95.82 $^4F_{9/2}$+2.41 $^4F_{7/2}$+1.31 $^2H_{11/2}$
46		15015.9	···	94.17 $^4F_{9/2}$+5.04 $^2H_{11/2}$+0.31 $^2H_{9/2}$
47		15029.0	···	95.79 $^4F_{9/2}$+2.76 $^2H_{11/2}$+0.89 $^2G_{7/2}$
48	$^2H_{11/2}$	15980.1	···	99.34 $^4H_{11/2}$+0.29 $^2G_{7/2}$+0.11 $^4F_{7/2}$
49	(16042.9)	16019.2	···	98.85 $^2H_{11/2}$+0.40 $^4F_{9/2}$+0.24 $^2G_{7/2}$
50		16038.4	···	98.22 $^2H_{11/2}$+1.09 $^4F_{9/2}$+0.23 $^4F_{7/2}$
51		16087.7	···	96.93 $^2H_{11/2}$+1.92 $^4F_{9/2}$+0.75 $^2G_{7/2}$
52		16116.6	···	99.11 $^2H_{11/2}$+0.54 $^4F_{9/2}$+0.17 $^2G_{7/2}$
53		16177.6	···	94.02 $^2H_{11/2}$+5.12 $^4F_{9/2}$+0.56 $^2H_{9/2}$
54	$^4G_{5/2}$	17069.9	···	89.54 $^4G_{5/2}$+7.48 $^2G_{7/2}$+1.97 $^4F_{3/2}$
55	(17166.6)	17178.6	···	49.68 $^4G_{5/2}$+49.07 $^2G_{7/2}$+0.35 $^2H_{11/2}$
56	$+^2G_{7/2}$	17312.9	···	52.06 $^2G_{7/2}$+45.27 $^4G_{5/2}$+1.68 $^4F_{5/2}$
57	(17433.5)	17399.9	···	80.11 $^2G_{7/2}$+18.63 $^4G_{5/2}$+0.33 $^2H_{11/2}$
58		17439.6	···	64.85 $^2G_{7/2}$+34.00 $^4G_{5/2}$+0.35 $^2H_{11/2}$
59		17482.9	···	73.89 $^2G_{7/2}$+24.78 $^4G_{5/2}$+0.50 $^4F_{7/2}$
60		17532.4	···	65.67 $^2G_{7/2}$+32.36 $^4G_{5/2}$+0.82 $^4F_{9/2}$

[a]Parameters from best fit are B_{20}=2452, B_{22}=410, B_{40}=2219, B_{42}=320+i57.6, B_{44}=−148−i186, B_{60}=435, B_{62}=−81.3+i253, B_{64}=−255+i122, B_{66}=266+i395 (cm^{-1}).

[b]State labels in the Russell–Saunders notation. Centroid energies are given below each state; values in parentheses are from aqueous solution data.

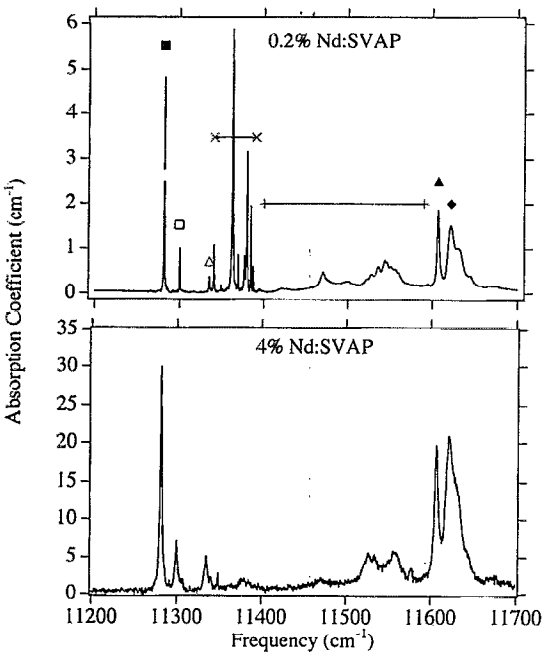

FIG. 3. $^4I_{9/2}\rightarrow{}^4F_{3/2}$ absorption coefficient for two concentrations of Nd^{3+} in SVAP. The sample temperature was 1.7 K. Markers indicate the lines or bands integrated for analysis in Fig. 4.

sulting main-site excitation spectrum is presented in Fig. 5 along with the absorption band, which it clearly follows. For all but the two lowest dye-laser frequencies indicated by the symbols in Fig. 5, emission from sites other than the main site is practically nonexistent.

The conclusion from Figs. 4 and 5 is that five $^4I_{9/2}\rightarrow{}^4F_{3/2}$ absorption lines arise from the main site. A natural interpretation is that the sharp line indicated by the solid triangle in Fig. 3 gives the frequency of the upper $^4F_{3/2}$ level and that the three broad overlapping lines under the solid diamond are Stokes phonon side bands of the line indicated by the solid square. The separation of zero phonon line and side bands in this interpretation is reasonable for optical phonon energies. A problem with this interpretation is that all

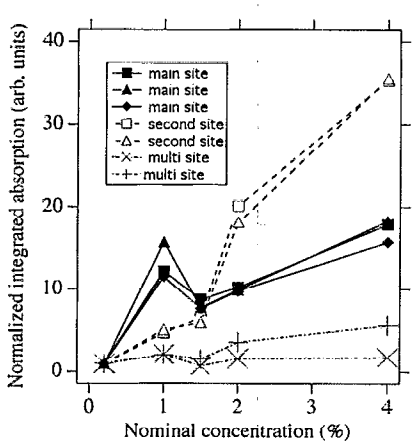

FIG. 4. Integrated absorption vs nominal concentration for lines or bands indicated in Fig. 3. To aid comparison, all curves are scaled to give the value unity at lowest concentration.

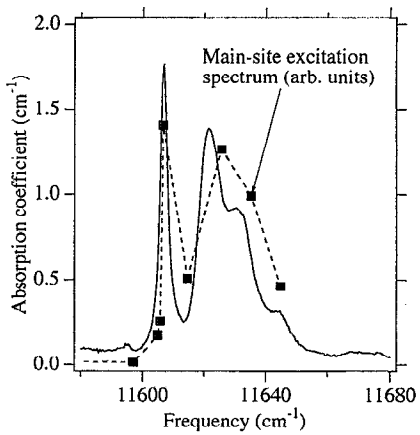

FIG. 5. Comparison of a portion of the $^4I_{9/2}\rightarrow{}^4F_{3/2}$ absorption spectrum (solid line) and the excitation spectrum for main-site emission (solid symbols). The sample temperature is 80 K.

four of the high-frequency main site lines appear together as thermal replicas of emission from the lower $^4F_{3/2}$ level at sufficiently elevated temperatures. Here, the broad lines would have to be anti-Stokes emission side bands, but there is no evidence of their Stokes counterparts, though these should be stronger. Hence, the phonon sideband interpretation remains in question. In Ref. 3 it is proposed instead that the strongest line under the solid diamond in Fig. 3 gives the upper $^4F_{3/2}$ level position since this feature appears to dominate the thermal replica emission spectrum. One of the purposes of performing the crystal-field calculation described below is to help decide which interpretation is correct. This calculation favors identifying the sharp line under the solid triangle in Fig. 3 as giving the position of the upper $^4F_{3/2}$ level.

Those features indicated by open symbols, referred to in Fig. 4 as "second site," increase together more rapidly with nominal concentration than do the main site lines. That the open-symbol features are sharp and distinct at all concentrations suggests that the crystal-field environment they belong to is also distinct, i.e., a distinct crystallographic site within the crystal, rather than just the main site perturbed by charge compensating defects. Luminescence transitions at the frequencies of the two second-site lines indicated are never clearly observed. Rather, at these two frequencies, sharp dips are observed in the broad luminescence profiles of other sites, presumably caused by second-site absorption of multisite emission.

The two groups of features indicated by × and + in Fig. 3 each have integrated strengths which are relatively constant. The apparent decrease in the peak heights of these lines with increasing concentration in Fig. 3 is due to broadening. Comparison with the site-selective emission data identify these bands with many of the luminescence lines which appear in addition to main-site emission. We refer to these as "multisite" bands. In addition to the total multisite concentration, the multiplicity of crystal-field environments is also independent of Nd concentration, as determined by 2 K site-selective experiments in the 4% sample. These obser-

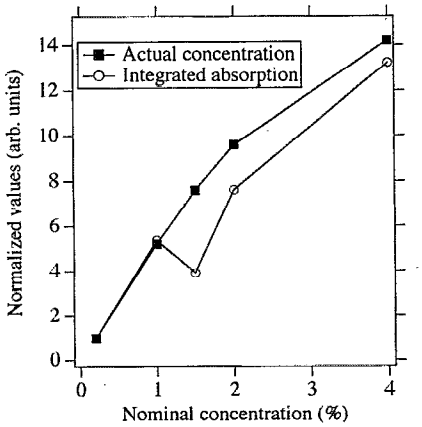

FIG. 6. Actual Nd concentration and total integrated $^4I_{9/2} \rightarrow {}^4F_{3/2}$ absorption vs nominal concentration. Both curves are scaled to give unity at [Nd]=0.2%.

vations contradict the first hypothesis given in the introduction. Though the proportion of multisites decreases, the absolute number and variety of them does not. Hence, broadband pumping efficiency of Nd:SVAP lasers will be reduced by the multisite presence at all Nd concentrations unless the multisites can contribute their absorbed energy to the mainsite via energy transfer (hypothesis 2).

To test our analysis of Fig. 3, we compare the sum of all integrations, which should equal the integral of the entire $^4I_{9/2} \rightarrow {}^4F_{3/2}$ band, to the actual concentration. Both quantities are plotted versus nominal concentration in Fig. 6, where each curve has been scaled to give unity at [Nd]=0.2%. For low concentration, the two curves are nearly identical, as they should be. That the absorption curve eventually drops below the concentration curve suggests that at high concentration some Nd is either optically inactive or contributes to a broad background which has escaped integration. Nonetheless, the total integrated absorption is always roughly proportional to actual concentration, which affirms our method of analysis above.

Our second hypothesis, that of preferential energy transfer to the main site, is explored next. Figure 7 presents $^4F_{3/2} \rightarrow {}^4I_{9/2}$ photoluminescence at 80 K for three concentrations and fixed excitation frequency. Solid symbols designate the five main-site lines. The remainder are multisite bands. As a measure of main-site emission strength, we integrate the lowest main-site line, since this line is far from any multisite band. For multisite emission, we integrate the group of lines indicated by the bracket. From Table I, it is clear that this group can contain no emission from the thermally populated upper $^4F_{3/2}$ level of the main site. Neither does it contain emission corresponding to the second-site transitions labeled by open symbols in Fig. 3.

The main-site:multisite luminescence ratio is compared with the main-site:multisite integrated absorption ratio as a function of nominal concentration in Fig. 8. Clearly, the main:multi emission ratio grows faster than the main:multi concentration ratio, which argues for energy transfer to the main site. For other excitation frequencies and choices of

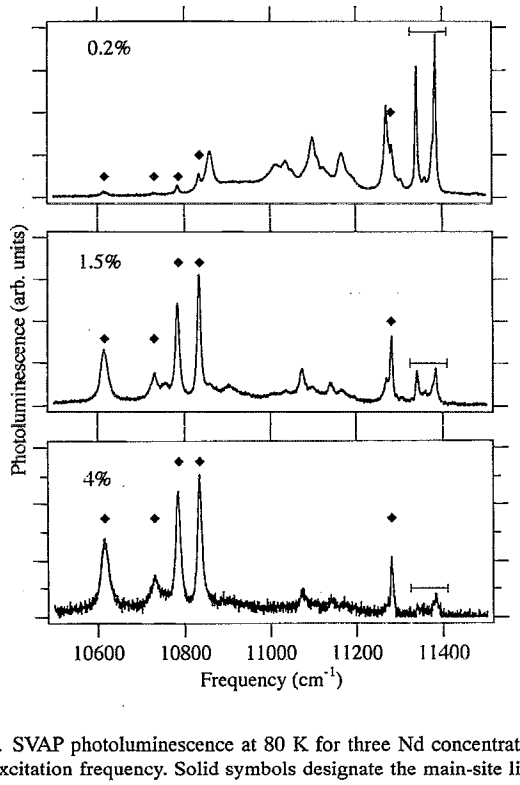

FIG. 7. SVAP photoluminescence at 80 K for three Nd concentrations and fixed excitation frequency. Solid symbols designate the main-site lines. The bracket indicates multisite lines integrated for analysis.

multisite lines, this difference in the rates of increase for the two ratios varies between a factor of 3 and 9. Such transfer was already suggested by Fig. 2, in which the main-site line appears for all excitation frequencies.

Since the lowest main site $^4F_{3/2}$ level is below that for any other site, the transfer is "down hill." Preferential transfer to the laser active site has been observed[5] also in the similar system Nd:fluorapatite [Nd:FAP], allowing the absorption of two extra sites to contribute to the population buildup in the main-site upper laser level. This favorable situation evidently holds also for Nd:SVAP, even with its considerably larger site multiplicity.

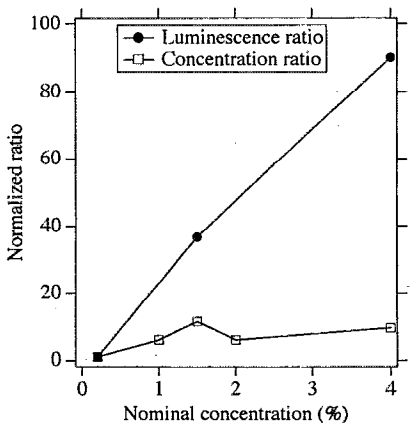

FIG. 8. Main:multi luminescence and integrated absorption (concentration) ratios vs nominal concentration. Both curves are scaled to give unity at [Nd]=0.2%.

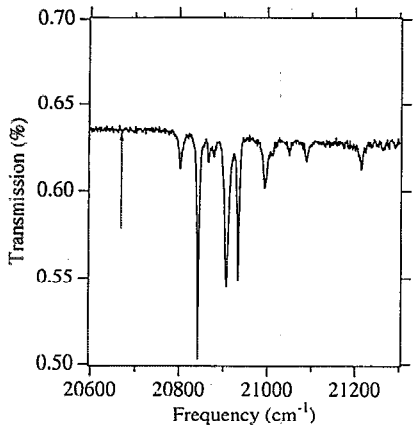

FIG. 9. Transmission spectrum of 2% Nd:SVAP at 80 K. The arrow shows the level position necessary for main-site excited-state absorption of the laser emission.

Down-hill transfer may be incomplete under practical lasing conditions since level differences between the main site and most of the multisites are less than kT at room temperature. In fact, the main:multi luminescence ratio with fixed-frequency excitation decreases by 30% in going from 1.7 to 80 K. (Line broadening and the appearance of additional lines from thermally populated multisite levels prevent straightforward integrations at 300 K.) Evidently, thermally activated back transfer competes with transfer to the main site. This suggests that at room temperature significant multisite population will exist in excited $^4F_{3/2}$ levels, even if only the main site is selectively excited.

Our visible absorption spectrum presented in Fig. 9 shows that no level is available for excited-state absorption (ESA) of laser emission (9386 cm^{-1}) from the upper laser level (11 278 cm^{-1} at 300 K), for otherwise an absorption line would appear at the position of the arrow. On the other hand, Fig. 9 reveals that absorption lines do occur at the necessary energy above multisite $^4F_{3/2}$ levels. Hence, absorption which originates in populated multisite $^4F_{3/2}$ levels is possible at the laser frequency, especially since such transitions tend to be broad at high concentration. This gives a possible loss mechanism for room-temperature lasing, a scenario presented schematically in Fig. 10.

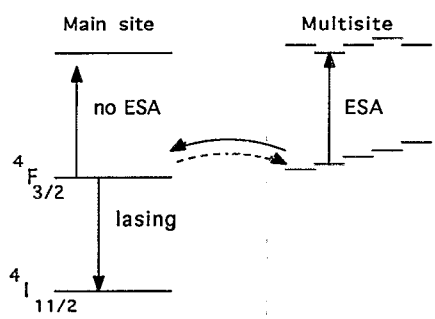

FIG. 10. Schematic for multisite excited-state absorption (ESA) of main-site laser emission. Transfer and backtransfer are shown by curved solid and dashed arrows, respectively.

III. CRYSTAL-FIELD CALCULATIONS

Calculations of the crystal-field split energy levels were performed for the lowest 13 multiplets of Nd^{3+} ($4f^3$) ion in a manner described previously.[6] The free-ion parameters E^k, ζ, α, β, and γ from Carnall *et al.*[7] for Nd^{3+} in aqueous solution and the resulting wave functions for the entire $4f^3$ electronic configuration of Nd^{3+} were used to calculate reduced matrix elements of the unit tensors, U^k (k=2,4,6). The reduced matrix elements involving the lowest 13 multiplets were then selected and were used in the calculation of the matrix elements of the crystal-field components. To compensate for the small errors introduced in the free-ion wave functions by using aqueous parameters, the centroid of each multiplet is allowed to vary freely to best fit the experimental data.

By analogy with the apatite crystal $Ca_5(PO_4)_3F$ (FAP), for which the Ca2 site is responsible for lasing,[5] the main site in SVAP is identified as the Sr2 site of C_{1h} symmetry. The crystal-field Hamiltonian for the Sr2 site in SVAP is given by

$$H_{\mathrm{CEF}}=\sum_{nm} B^*_{nm}\sum_i C_{nm}(i) \tag{1}$$

and

$$C_{nm}(i)=\sqrt{4\pi/(2n+1)}\,Y_{nm}(\theta_i,\varphi_i);$$

$$C_{n,-m}(i)=(-1)^m C^*_{nm}(i),$$

which for C_{1h} symmetry we have the requirement that $n+m$ must be even. For n even, we have: n=2, m=0, 2; for n=4, m=0, 2, 4, and for n=6, m=0, 2, 4, 6. This gives 15 crystal-field parameters (the B_{nm} for $m\neq 0$ are, in general, complex) and this, in general, can be reduced to 14 by a simple rotation about the crystallographic c axis to make B_{22} real and positive.[8] In order to determine the crystal-field parameters from the experimental data, we must have reasonably good starting values of B_{nm}. To obtain starting values for the B_{nm}, we use the point charge model.[6]

A. Lattice sums for A_{nm}

In the three parameter theory of crystal fields,[9] the crystal-field parameters B_{nm} are related to the crystal-field components A_{nm} by

$$B_{nm}=\rho_n A_{nm}, \tag{2}$$

where the ρ_n are rare-earth ion dependent, host independent, effective radial factors (Ref. 8, Chap. 13). In this model, the point-charge crystal-field components are given by

$$A_{nm}=-e^2\sum_j q_j \frac{C_{nm}(\hat{R}_j)}{R_j^{n+1}}, \tag{3}$$

where q_j is the charge (in units of the electron charge) on the ion at R_j and the sum covers all ions in the solid (usually all the ions in 2 or 3 unit cells). In order to perform the sum in Eq. (3), the detailed x-ray data (the position of all the ions in a unit cell) are necessary. To our knowledge, such data for SVAP have never been published, but we do have the detailed x-ray data on $Ca_5(PO_4)_3F$ (FAP)[10] and the cell size for SVAP,[11] which is reported to have the same space group, $C^2_{6h}(P6_3/m)\#176$. We used this combination to calculate

TABLE II. Crystal-field components A_{nm} (cm^{-1} $Å^n$) and calculated crystal-field parameters B_{nm} (cm^{-1}) for the Sr2 site (C_{1h}) in $Sr_5(VO_4)_3F$.[a]

nm	Re A_{nm}	Im A_{nm}	Re B_{nm}(Nd)	Im B_{nm}(Nd)
20	7643	···	1304	···
22	1927	0	328.8	0
40	1404	···	811.0	···
42	−1822	1570	−1052	960.8
44	−133.6	−1614	−77.16	−932.4
60	59.86	···	95.16	···
62	240.6	120.6	382.4	191.6
64	133.4	11.01	180.2	17.50
66	13.61	105.8	21.64	168.1

[a]Cell size from Grisafe and Hümmel (Ref. 11) for $Sr_5(VO_4)_3F$ and the position of ions in the unit cell from Hughes *et al.* (Ref. 10) for $Ca_5(VO_4)_3F$. The charge on the oxygen ions was taken at −1.8 and vanadium at 4.2; all others are at their valence values.

the even n A_{nm} given in Table II. That is, the cell size of SVAP from Grisafe and Hümmel[11] was used with the fractional positions of the ions in the unit cell given by Hughes *et al.*[10] for FAP. In the VO_4^{-3} complex, the charge on the vanadium site was assumed to be covalent such that $4q_o+q_v=-3$ with $q_o=-1.8$ and $q_v=4.2$, which maintains the charge on the VO_4 complex at −3. The choice of $q_o=-1.8$ was taken from the value of the oxygen charge in $Y_3Al_5O_{12}$ for the tetrahedral AlO_4 complex which best fit the theoretical A_{nm}, with the experimental A_{nm}^{exp} determined by $A_{nm}^{exp}=B_{nm}/\rho_n$ with B_{nm} the best-fit crystal-field parameters for Nd^{3+} in YAG.[12]

B. Energy level calculations

Starting values of the crystal-field parameters in the fitting of the experimental levels were taken from Table II. The first calculation was done with one energy level from each multiplet and with the centroids varied to fit the experimental data. The subsequent fittings were done by gradually adding in experimental energy levels. Finally, all the energy levels were entered except the highest energy level of the $^4F_{3/2}$, and the resulting splitting of this level was predicted to be 314.3 cm^{-1} with the rms deviation of 6.1 cm^{-1} after more than 100 iterations. A comparison with the possible experimental splittings of 340.4 or 325.4 cm^{-1}, as discussed above, shows the smaller experimental value is much closer to the theoretical value. Hence, the absorption line at 11 607 cm^{-1} was chosen to give the main site upper $^4F_{3/2}$ level, and this level was used for the final fitting. After more than 100 iterations, the best fit was obtained and is given in Table I. The best-fit parameters are (all in cm^{-1} units)

$$B_{20}=2452, \quad B_{22}=410,$$

$$B_{40}=2219, \quad B_{42}=320+i57.6,$$

$$B_{44}=-148-i186,$$

$$B_{60}=435, \quad B_{62}=-813+i253,$$

$$B_{64}=-255+i122, \quad B_{66}=266+i395$$

with an rms deviation of 6.1 cm^{-1}.

A comparison of these crystal-field parameters with those given in Table II shows significant differences, which may result from the approximation that the fractional positions of the ions in the unit cell are the same as FAP. A second possible explanation is the charge compensation which must be present when Sr^{2+} is replaced by Nd^{3+}. If the charge compensation mechanism is $Sr^{2+}\rightarrow Nd^{3+}$ and $F^-\rightarrow O^{-2}$, then since the nearest neighbor (2.46 Å) to the Sr^{2+} in the Sr2 site is F^- (which becomes an O^{-2} ion), this change can have a considerable impact on the parameters of that site. This is only one of the possible ways that charge compensation could take place, and there are many possible other ways as indicated by the richness of the optical spectra.

IV. SUMMARY

To summarize, Fourier-transform photoluminescence spectroscopy with selective excitation reveals a large number of crystal-field environments for Nd^{3+} ions in $Sr_5(VO_4)_3F$. Preferential energy transfer to the lasing site has been observed, but loss may occur because of back transfer at room temperature. A crystal-field analysis has been performed for the levels of the lasing site with good agreement between the experimental and calculated energy level spectrum. The experimental methods used in this work, Fourier-transform photoluminescence spectroscopy with selective excitation, are generally applicable to other transfer problems in multisite, as well as frequency converting, laser crystals.

ACKNOWLEDGMENTS

This work was supported by the Division of Sponsored Research and Teaching at the University of Central Florida and by the Air Force Office of Scientific Research. The authors thank Pin Hong for assistance with some of the measurements.

[1] S. A. Payne, B. H. T. Chai, W. L. Kway, L. D. DeLoach, L. K. Smith, G. Lutts, R. Peale, X. X. Zhang, G. D. Wilke, and W. F. Krupke, Conference on Lasers and Electro Optics (CLEO), Baltimore, 1993, postdeadline paper.

[2] B. H. T. Chai, G. Loutts, J. Lefaucheur, X. X. Zhang, P. Hong, M. Bass, I. A. Shcherbakov, and A. I. Zagumennyi, *OSA Proceedings on Advanced Solid State Lasers,* edited by T. Y. Fan and B. H. T. Cahi (Optical Society of America, Washington, DC, 1994), pp. 41–52.

[3] P. Hong, X. X. Zhang, R. E. Peale, H. Weidner, M. Bass, and B. H. T. Chai, J. Appl. Phys. (to be published).

[4] C. D. Orth, S. A. Payne, and W. F. Krupke, *OSA Proceedings on Advanced Solid State Lasers,* edited by T. Y. Fan and B. H. T. Chai (Optical Society of America, Washington, DC, 1994), pp. 280–282.

[5] K. B. Steinbruegge, T. Henningsen, R. H. Hopkins, R. Mazelsky, N. T. Melamed, E. P. Riedel, and G. W. Roland, Appl. Opt. **11**, 999 (1972).

[6] C. A. Morrison and R. P. Leavitt, J. Chem. Phys. **71**, 2366 (1979).

[7] W. T. Carnall, P. R. Fields, and K. Rajnak, J. Chem. Phys. **49**, 4424 (1968).

[8] C. A. Morrison, *Angular Momentum Theory Applied to Interactions in Solids,* Lecture Notes in Chemistry No. 47 (Springer, Heidelberg, 1988).

[9] R. P. Leavitt, C. A. Morrison, and D. E. Wortman, "Rare-Earth Ion-Host Interactions: 3. Three-Parameters Theory of Crystal Fields," Harry Diamond Laboratories Report, HDL-TR-1673, June 1975.

[10] J. M. Hughes, M. Cameron, and K. D. Crowley, Am. Mineral. **74**, 870 (1989).

[11] D. A. Grisafe and F. A. Hümmel, J. Solid State Chem. **2**, 160 (1970).

[12] E. Filer, C. A. Morrison, G. Turner, and N. P. Barnes, in *OSA Proceedings on Advanced Solid State Lasers*, edited by H. P. Jensen and G. Dube (Optical Society of America, Washington, DC, 1990), pp. 354–370.